American Mineralogist, Volume 96, pages 1373–1380, 2011

A new type of high-pressure low-flow metering valve for continuous decompression: First experimental results on degassing of rhyodacitic melts

Marcus Nowak,[1,*] Sarah B. Cichy,[2] Roman E. Botcharnikov,[2] Norbert Walker,[1] and Willi Hurkuck[2]

[1]Fachbereich Geowissenschaften, Universität Tübingen, Wilhelmstrasse 56, 72074 Tübingen, Germany
[2]Institut für Mineralogie, Leibniz Universität Hannover, Callinstrasse 3, 30167 Hannover, Germany

Abstract

A novel type of high-pressure low-flow metering valve has been designed for experiments at continuous decompression in internally heated pressure vessels (IHPV) at pressures up to 500 MPa and temperatures up to 1500 °C. It consists of a modified high-pressure valve coupled with a piezoelectric nanopositioning system. The piezoelectric actuator (1) positions the needle of the valve statically with very high precision on a nanometer scale for infinitesimally slow decompression and, alternatively, (2) opens and closes the valve completely, within milliseconds, to achieve a fast pressure drop only limited by the diameter of the high-pressure tubing and the entire volume of the autoclave system.

The valve connected to an IHPV has been successfully tested to simulate continuous decompression of volatile-bearing magma. Water saturated rhyodacitic melt was synthesized at 1050 °C and 300 MPa and subsequently decompressed to 50 MPa at an integrated decompression rate of 0.28 MPa/s using continuous decompression as well as single-step and multi-step decompression techniques. The experimental results of the three methods show significant differences, having important implications for the interpretation of textures observed in natural volcanic rocks. Bubble number density (BND) values increase from continuous to multi-step and to single-step decompression by two orders of magnitude. Bubble size distribution (BSD) also differs significantly. The BSD curve of the single-step decompression shows largest variation both in size and in population number density, whereas the BSD trend for the sample of multi-step decompression shows the smallest variation between size and population density of bubbles. The BSD of the continuously decompressed sample indicates similar proportions of bubbles with different size. Channel formation in the sample of single-step decompression may indicate fluid escape from over-pressurized bubbles through the melt. Single-step and continuous decompression style represent two extreme cases of magma degassing in which bubble nucleation and bubble growth are predominant processes, respectively, whereas multi-step decompression resembles the intermediate case.

Keywords: Silicate melt, continuous degassing, bubble nucleation, bubble growth, high-pressure valve

Introduction

Most physicochemical processes occurring during magma ascent are kinetically controlled. These processes are not directly observable in nature. However, they can be investigated in the laboratory by conduction of decompression experiments simulating magma ascent from depths of magma chamber to the Earth's surface. The quantitative information obtained in the experiments is necessary to understand the coupling of physicochemical and rheological properties of magma and *P-T-t* conditions. In principle, pressure decrease unbalances a volatile bearing magma (essentially H_2O and CO_2, H_2S, SO_2, halogens, and noble gasses; e.g., Symonds et al. 1994) out of equilibrium. Readjustment can lead to a separation of fluid and melt phases by overstepping the fluid saturation limit. This results in a complex interaction between different processes of nucleation, growth, coalescence, and segregation of fluid bubbles accompanied by changing viscosity and decreasing density of the magma, which are the driving forces for accelerated magma ascent (e.g., Woods 1995; Gonnermann and Manga 2007) that can control the eruption style (e.g., Hawkesworth et al. 2004; Miller and Wark 2008).

Fast decompression experiments of volatile-bearing silicate melts are necessary for studying the process of bubble nucleation, which is the formation of a new phase in relation to a specific supersaturation, relegated by forces that act against a new boundary (surface tension). Hence, to understand the process of nucleation, a steady supersaturation achieved by fast pressure drop needs to be applied (e.g., Gardner 2007a; Hamada et al. 2010). Furthermore, fast shock-wave-like decompression is essential in studying near surface fragmentation processes induced by abrupt decompression from high-pressure to ambient conditions (e.g.,

* E-mail: marcus.nowak@uni-tuebingen.de

Alidibirov and Dingwell 1996; Spieler et al. 2004; Scheu et al. 2006). However, these investigations do not give full insight into dynamic decompression processes with volatile release prior to eruption. To elucidate these dynamic processes during magma ascent there is a need for decompression experiments with controlled and realistic small decompression rates.

State of the art

The majority of published results from decompression experiments were obtained from experiments conducted using a stepwise decompression method. At high pressure a conventional needle valve is opened for a short time. As a consequence, pressure drops rapidly at about 2.5 to 10 MPa/s, equivalent to unrealistic magma ascent velocities of 300 to 1200 km/h assuming a crustal density of 3 g/cm^3, but then remains constant at a reduced pressure for a certain time. Shock-wave-like pressure drop with subsequent equilibration time at reduced pressure was used to simulate "pseudo-continuous" decompression rates by e.g., Hurwitz and Navon (1994), Martel and Schmidt (2003), Mastrolorenzo and Pappalardo (2006), and Gardner (2007a, 2007b).

To study magma-degassing and crystallization processes, Mastrolorenzo and Pappalardo (2006) performed a set of multi-step decompression experiments with Campanian Ignimbrite (CI) trachyte at 950 °C and initially water-saturated conditions. Compositional and textural features of the experimental products were compared with natural samples from volcanic deposits. The results provide the idea that fast ascent rates result in closed system degassing, which causes magma fragmentation and an explosive eruption style, whereas slow ascent rates result in open system degassing inducing mild explosive to effusive eruption style. In a closed system, the bubble number density (BND) increases and the gas in a bubble expands during pressure release. By reaching a critical volume fraction, bubbles interact and coalesce (Gardner 2007a, 2007b). At a certain threshold, neighboring bubbles interconnect forming gas channels in the magma. The gas can gush through the channel network producing permeable open-system conditions of magma degassing on decompression. The transition between closed and open system degassing can be crucial for the effusive or explosive eruption style (Herd and Pinkerton 1997; Gonnermann and Manga 2005). As a rule of thumb, gas bubbles in slowly ascending magma have sufficient time to coalesce, whereas rapidly rising magma erupts explosively (Woods and Koyaguchi 1995; Mastrolorenzo and Pappalardo 2006). Thus, it is suggested that decompression rate is the critical parameter that influences the coupled dynamic processes and as a consequence the eruptive style of volcanoes.

Up to now only few continuous decompression experiments of hydrous melts above liquidus temperature with realistic decompression rates have been realized. To our knowledge, only 12 decompression experiments with hydrous rhyolitic melt above liquidus temperature using slow real continuous decompression with a rate of 0.003–8.5 MPa/s have been performed by Mangan and Sisson (2000). They used a complex system of needle valves and high-pressure capillaries to maintain continuous bleeding of the autoclave. However, problematic was the small sample diameter of 2 mm allowing significant diffusive volatile loss from the sample rim, and hence supersaturation was mitigated.

Recently, Brugger and Hammer (2010) performed a set of subliquidus, continuous decompression experiments in externally heated cold-seal pressure vessels at 880 °C with a continuous pressure-time trajectory of 0.5–10 MPa/h, initiated from 130 MPa, to study crystallization kinetics of plagioclase. They showed that the decompression path influences crystal texture, based on comparisons between multi-step and continuous decompression experiments. Plagioclase crystals in multi-step decompression runs are skeletal, whereas in continuous decompression runs crystals are faceted suggesting diffusion-limited growth and interface reaction controlled growth, respectively.

The interpretation of volcanic products regarding magma storage and magma ascent in deeper zones of volcanic systems is vague and at best qualitative due to a lack of continuous decompression experiments. Magmatic processes at pressures of the Earth's crust can be successfully simulated in internally heated pressure vessels (IHPV) but up to now a suitable high-pressure low-flow metering valve in conjunction with IHPV was not available. The purpose of this pilot study is to demonstrate the operational capability of our newly developed valve to allow controlled slow release of argon from an IHPV even at $P > 200$ MPa and $T > 950$ °C. At such conditions, the continuous magma ascent from reservoir to subsurface levels can be simulated for magmas with compositions more mafic than rhyolites. Achievement of such high *P*-*T* conditions and the investigation of mafic melt compositions were not possible in cold-seal pressure vessels mostly used by the previous workers. Our first results demonstrate that different styles of decompression generate different bubble nucleation and growth conditions in hydrous rhyodacitic melt.

Experimental setup

The valve

We developed a prototype of a novel high-pressure low-flow metering valve (Fig. 1), equipped with a piezoelectric nanopositioning system ensuring slow continuous pressure release from IHPV. The piezoelectric actuator is capable of (1) positioning the needle of the high-pressure valve statically with very high precision on a nanometer scale for continuous slow pressure release and, alternatively, (2) opening and closing the valve completely within milliseconds to achieve fast pressure drops limited only by the diameter of the high-pressure tubing. A 1 GPa Nova Swiss high-pressure valve was modified to minimize friction of the needle. Tight polytetrafluoroethylene seals were replaced by a thin rubber seal and polished

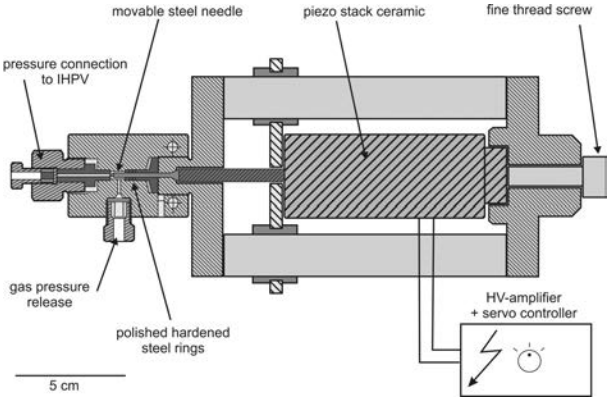

Figure 1. Schematic drawing of the new high-pressure low-flow metering valve.

steel rings that guide perfectly the steel needle. The nanopositioning system for the valve needle consists of three parts: (1) A power piezo stack actuator (Physik Instrumente GmbH) with a travel range of 120 µm; (2) a flexible tip (Physik Instrumente GmbH) screwed into the top piece of the translator to decouple lateral forces, because PZT (modified lead zirconate titanate) ceramic stacks cannot withstand bending forces; (3) a fine thread screw that is used for pre-adjustment of the piezo stack on a 10 µm scale.

A coupling, made of stainless steel, connects the valve with the power piezo stack actuator. The flange of the high-pressure valve and the flange of the actuator are force-fitted by two steel poles. The piezo stack is guided precisely by two slide bearings surrounding the steel poles to minimize lateral tilt. A high-power 1000 V piezo amplifier equipped with a 10 turn potentiometer (Physik Instrumente GmbH) is used to drive the piezo actuator equipped with a servo controller module for closed loop piezo position control. A 360° turn of the potentiometer is equivalent to 12 µm travel length of the valve needle. As a simple method to control the decompression rate, the gas released from the valve was directed through the HPLC plastic tube connected to the bottom of a water-filled glass column to be able to observe and count the ascending gas bubbles. The combination of this simple visual control on the number of bubbles with the pressure values read from the pressure transducer of the IHPV enables easy correction for the desired rate of decompression.

First continuous decompression experiments

The piezoelectric driven valve is connected to an IHPV. High-temperature advancement of the IHPV furnace allows maximum temperature of 1500 °C, a pressure of 500 MPa can be reached routinely (e.g., Nowak et al. 2004), and samples can be quenched rapidly within seconds. This allows investigating the physicochemical properties of even strongly depolymerized tholeiitic and alkali-rich volatile-bearing basaltic systems (e.g., Berndt et al. 2002; Stelling et al. 2008; Giordano et al. 2008; Freise et al. 2009; Spickenbom et al. 2010). The piezoelectric driven valve was tested successfully to a pressure load of 500 MPa. First decompression tests at pressures up to 500 MPa demonstrate that infinitesimally small decompression rates (<10 Pa/s) up to high decompression rates (>10 MPa/s) that are limited by the capillary diameter can be realized. Although it takes the same molar amount of argon gas to change pressure from 300 to 260 MPa than it does from 100 to 60 MPa as argon is lost from the vessel, the rate of gas loss will decrease with decompression due to the elastic stress/strain response of the valve system. Therefore, the valve needle was driven back carefully using the potentiometer of the piezo amplifier during decompression to keep the released number of gas bubbles per time interval in the water column in first approximation constant. This readjustment is reflected in Figure 2 by the slightly uneven *P-t* path of the continuous decompression.

Starting material for decompression experiments

A synthetic analog of a rhyodacitic silicate melt (Table 1) was used as starting material. This composition was already investigated in several studies related to Unzen volcano (Sato et al. 1999, 2005; Botcharnikov et al. 2004; Cichy et al. 2011).

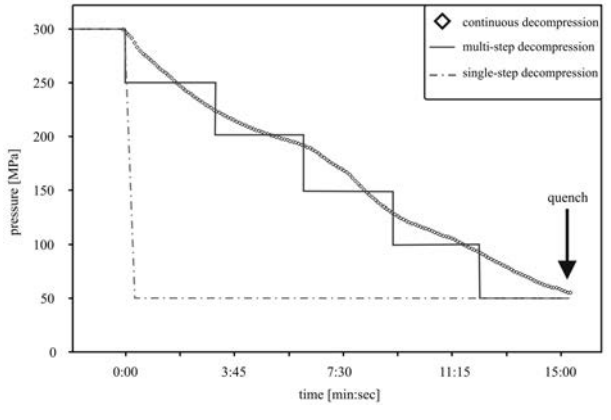

Figure 2. Schematic diagram showing the differences of the *P-t* paths between continuous decompression (diamond symbols), multi-step decompression (solid line), and single-step decompression (dashed line) at experimental conditions of 1050 °C in the H_2O-saturated system.

Table 1. Glass compositions, experimental parameters, and results of decompression experiments

	Synthetic rhyodacitic starting glass	DEC11syn	DEC11-5	DEC11-6	DEC11-8
Starting pressure (MPa)	(dry)	300	300	300	300
Final pressure (MPa)	–		50	50	50
Decompression rate (MPa/s)	–		0.28	0.28	0.28
Decompression method	–	isobaric	continuous	multi-step	single-step
No. of decompr. steps	–	–	–	5	1
Pressure drop per decompression step (MPa)	–	–	–	50	250
Glass composition in (wt%)					
SiO_2	69.95	65.99 (0.26)	68.71 (0.25)	69.02 (0.22)	69.80 (0.38)
TiO_2	0.50	0.47 (0.04)	0.50 (0.04)	0.52 (0.05)	0.51 (0.05)
Al_2O_3	14.21	13.17 (0.18)	13.89 (0.25)	13.96 (0.14)	13.88 (0.15)
FeO	3.57	3.51 (0.24)	3.95 (0.16)	3.41 (0.24)	3.26 (0.36)
MnO	0.12	–* (–)	–* (–)	–* (–)	–* (–)
MgO	1.44	1.48 (0.13)	1.47 (0.10)	1.56 (0.07)	1.58 (0.15)
CaO	4.05	3.86 (0.19)	3.96 (0.11)	4.18 (0.14)	4.08 (0.14)
Na_2O	3.16	2.72 (0.12)	3.13 (0.15)	3.19 (0.12)	3.20 (0.16)
K_2O	2.75	2.48 (0.11)	2.68 (0.12)	2.65 (0.12)	2.74 (0.14)
H_2O (NIR)	–	7.46 (0.32)	3.01 (0.31)	2.76 (0.29)	2.32 (0.31)
Textural analyses					
Vesicularity (vol%)	–	<0.50	63.67	44.45	23.22
log BND (mm^{-3}) after Gardner et al. (1999)	–	– –	2.22 (0.16)	3.50 (0.16)	4.40 (0.34)

Note: Numbers in parentheses show the standard deviation (1σ) of replicated analyses.
* Not determined (MnO contents of decompression products were below detection limit).

It corresponds to the groundmass composition of the magma erupted by Unzen volcano in 1991–1995, and hence, our decompression experiments are focused on the evolution of the final melts during the eruption.

For the glass preparation, a mixture of oxides (SiO_2, TiO_2, Al_2O_3, Fe_2O_3, MnO, and MgO) and carbonates ($CaCO_3$, Na_2CO_3, and K_2CO_3) was ground in a rotary mortar. The mixed powder was melted for 2 h in platinum crucible at 1600 °C, 1 atm in air ($\log f_{O_2} = -0.68$). Afterward, the melt was quenched to glass by placing the crucible into a water bath. To improve the homogeneity of the batch, the glass was ground again in the agate mortar and re-melted for 0.5 h at the same *P-T* conditions. Cylinders with diameter of ~2.5 mm and length of ~3 mm were drilled out of the quenched glass.

High-pressure experiments

Cylinders of dry glass were loaded with about 10 wt% H_2O into $Au_{80}Pd_{20}$ capsules (2.5 cm long, 2.8 mm inner diameter) and welded shut. The amount of water was chosen to be sufficient to saturate all melts at given *P* and *T*. The capsule was placed in an Ar-pressurized IHPV at oxygen fugacity corresponding to a range between $\log f_{O_2}$ ~ QFM +1.0 to QFM +1.7 (QFM = quartz fayalite magnetite buffer), which was achieved by addition of hydrogen gas to argon. After a synthesis for four days at the *P* and *T* conditions of 300 MPa and 1050 °C, the synthesis capsule (DEC11syn, Table 1) was quenched rapidly by dropping it into the cold zone of the sample holder. The quench rate was about 150 °C/s. After quenching, the hydrated glass cylinder was cut into four small glass cylinders (~0.5 cm length each). Finally, these fluid-saturated glass cylinders were individually inserted into $Au_{80}Pd_{20}$ capsules (~1.5 cm length), which were welded shut and loaded into the IHPV. After a short annealing time of two hours at 300 MPa and 1050 °C, an isothermal decompression to the final pressure of 50 MPa was initialized. After reaching the final *P*, the capsules were rapidly quenched. Cylindrical cores with a diameter of 2.0 mm were drilled out of the quenched experimental products for X-ray tomography. In addition, thin sections were prepared for electron microprobe and FTIR analyses.

To investigate how the style of decompression affects the processes of bubble

formation we applied three different decompression methods with a "constant" time-integrated decompression rate of 0.28 MPa/s equivalent to an ascent rate of 34 km/h using a rock density of 3 g/cm^3: single-step decompression, multi-step decompression, and continuous pressure release (Fig. 2). For single-step decompression (sample DEC11-8), the entire pressure of 250 MPa was instantaneously released from 300 MPa down to final 50 MPa within a few seconds (2500 bar in ~20 s = 12.5 MPa/s = 1500 km/h ascent velocity) and then the capsule was held at the final pressure for the next 15 min before quenching. For multi-step decompression (sample DEC11-6), pressure was released in five equal steps of 50 MPa with an interval of three minutes also with a decompression rate of 12.5 MPa/s. The continuous decompression from 300 to 50 MPa (sample DEC11-5) equivalent to 34 km/h was conducted for 15 min, using the high-pressure piezoelectric decompression valve, which is described in this paper. The pressure release can lead to a significant cooling of the gas and the sample depending on decompression rate and on pressure difference. In a recent study, Hamada et al. (2010) documented a maximum cooling of the sample of 35 °C at similar experimental conditions. However, during our decompression experiments the temperature fluctuation of the samples were kept constant within 10 °C due to the fast response of the internal heating furnace. Furthermore, Hamada et al. (2010) demonstrate that temperature has an insignificant effect on BNDs in hydrous rhyolitic melt at a given decompression rate. Thus, our samples should not be affected by small temperature fluctuations within 10 °C.

Analytical methods

Electron microprobe analysis (EMPA)

Major element composition of the experimental glasses was analyzed with a Cameca SX-100 microprobe using 15 kV as the acceleration voltage. Glass analyses were conducted with 4 nA beam current, a defocused electron beam (5–10 µm diameter), and peak counting times of 4 s for Na and K and 8 s for the other elements. Ten measurements were made for each sample to reduce possible analytical errors and to check the homogeneity.

Fourier transform infrared spectroscopy (FTIR)

Fourier transform infrared spectroscopy (FTIR) was used to estimate concentration of dissolved water in the experimental glasses, using a Bruker IFS88 FTIR spectrometer with a connected IRscopeII microscope. For NIR (near infrared) analysis we used a tungsten light source, a CaF_2-beam splitter and a MCT-detector. The spectral resolution was 4 cm^{-1}. One hundred scans per background and per sample were collected. The analyzed area was 80 × 80 µm. The H_2O concentrations were calculated from the heights of the peaks at 5200 cm^{-1} due to dissolved molecular water and 4500 cm^{-1} due to OH, using a tangential baseline correction. The extinction coefficients for the calculation of water concentration in the glasses were estimated using an empirical calibration of Ohlhorst et al. (2001) and they varied from 1.34 to 1.36 L/(mol·cm) for the 5200 cm^{-1} peak and from 1.13 to 1.15 L/(mol·cm) for the 4500 cm^{-1} peak. Since the compositions of glasses were close to rhyolites, glass densities were calculated applying the empirical calibration after Withers and Behrens (1999). Sample thicknesses were determined with a Mitutoyo digital micrometer (precision of ±2 µm). The thicknesses varied between 80 and 90 µm. Care was taken to choose areas either without or with very few bubbles. The average total H_2O concentrations of NIR measurements repeated at three different locations of the samples are shown in Table 1.

Image and textural analyses

The cylinders of glasses (2.0 mm in diameter; 2–5 mm in length) were analyzed at the synchrotron light source (SLS) of the Paul-Scherrer-Institute in Villigen, Schwitzerland. The beamline for tomographic microscopy and coherent radiology experiments ("TOMCAT") receives photons from a 2.9 T superbending magnet with a critical energy of 11.1 keV and produces a monochromatic beam. This non-destructive synchrotron-based X-ray micro-tomography was used to record digitalized projection images (256 gray levels) of the samples. The images have a resolution of 2048 × 2048 pixels, while one pixel is represented by 0.37 µm in size at a magnification of 20×. Grayscale of the images represents the variation in density of the analyzed material (Figs. 3a–3d, left side). To enhance the visual contrast between glass and bubbles in the images, we manually marked the bubbles in our images in black color (Figs. 3a–3d, right side). To reduce noise, a filter ("Parzen") was used for the reconstruction and smoothing of the images. Due to rim effects, the images were cropped and reduced to the actual inner image circle, having a diameter of 2048 pixel equal to 0.758 mm (Figs. 3a–3d). These corrected images were used to identify the morphology of bubbles and to quantify their textural characteristics within the experimental products, applying the public computer program ImageJ (http://rsb.info.nih.gov/ij). The image analysis provided information about total area, average size, area fraction, as well as about the width, length, and circularity of each vesicle. The detection limit for the bubble size depends on the magnification and on the resolution of the digitalized BSE pictures.

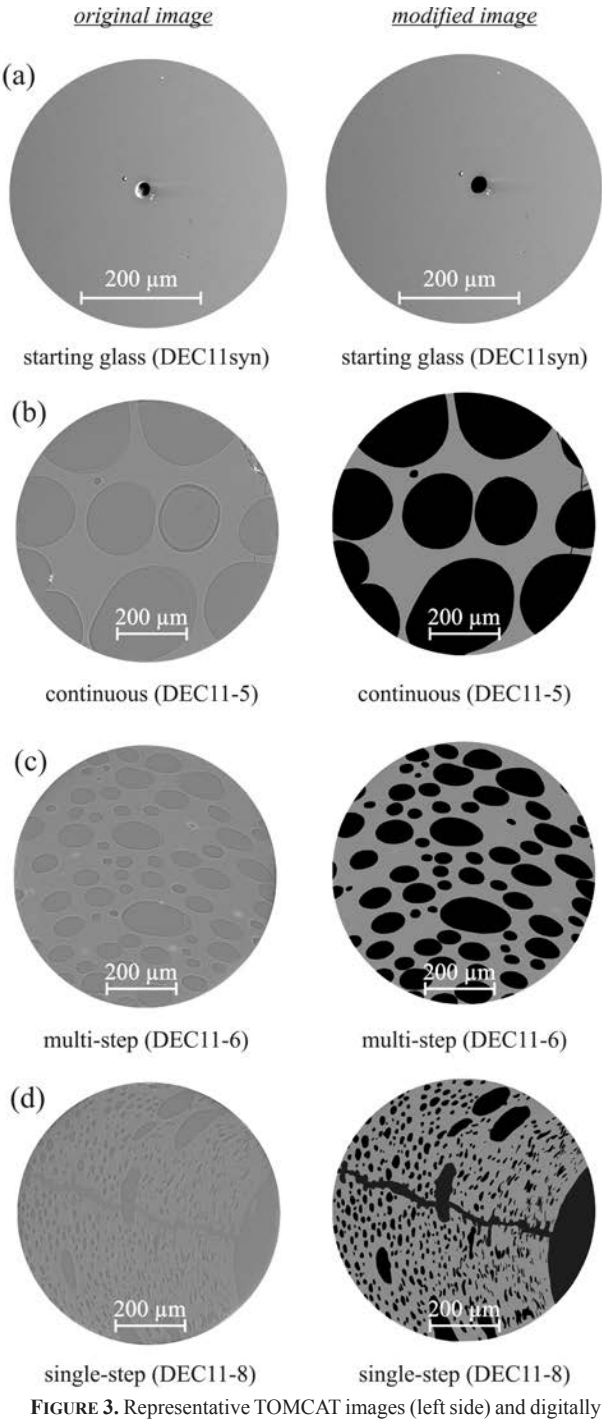

Figure 3. Representative TOMCAT images (left side) and digitally processed images (right side) of the (**a**) starting glass (DEC11syn) and of the experimental end-products of (**b**) continuous decompression (DEC11-5), (**c**) multi-step decompression (DEC11-6), and (**d**) single-step decompression (DEC11-8).

For the characterization of the experimental products, 2–4 different images at different positions within the sample were analyzed for each sample to minimize the truncation effect (e.g., Armienti 2008).

The geometric information (e.g., heights, width, and area of each single bubble, vesicularity of the sample, etc.) obtained by ImageJ analysis was used to determine textural characteristics such as BSD as well as BND. The BSD values were determined following the methods of Higgins (2000, 2002, 2006a, 2006b) by using the CSDcorrections1.3.8 software (http://wwwdsa.uqac.ca./~mhiggins/csd-corrections. html). The bubble-size distribution of a rock is the number of bubbles per unit volume within a series of defined size intervals. The population density (n) is defined as the number of bubbles in a given size class per unit volume, where N is the total number of bubbles of size less than R, and R is some characteristic bubble size (Marsh 1988):

$$n = \frac{dN}{dR} \quad (1)$$

BND refers to the number of bubbles per unit volume. The BND determination was based on the method of Gardner et al. (1999). The volumes of individual bubbles were determined by assuming that bubbles have an ellipsoidal shape. The volume of such ellipsoidal bubble was calculated from the major and minor length given by ImageJ analysis:

$$V_{\text{ellipsoid}} = \tfrac{4}{3}\pi a^2 b \quad (2)$$

where a and b represent the major and minor lengths of the ellipse, respectively.

The BND was calculated as:

$$BND = \frac{\varphi_m}{\sum \frac{n_i}{N_T} V_i} \quad (3)$$

where n_i and V_i are the number and volume of bubbles of diameter i, respectively, N_T is the total number of bubbles measured, and Φ_m is the measured volume fraction of the vesicles.

RESULTS

The silica-rich (66 wt% SiO_2) and water-saturated (7.5 wt% H_2O) starting glass (DEC11syn) contains only a few crystals (oxides) and bubbles (total porosity less than 0.5 vol%; Fig. 3a). The chemical melt compositions of the end-products of all three different decompression methods are similar within the uncertainties for all major elements. Vesicularities of the decompression end-products range from 23.2 vol% (single-step) to 44.5 vol% (multi-step) and to 63.7 vol% (continuous), see Table 1. The water content of the residual melt decreases with changing decompression from continuous (3.01 wt%) to multi-step (2.76 wt%) and to single-step (2.32 wt%) path (Table 1; Fig. 4a). For comparison, water solubility of high-silica melts (1050 °C) can be derived from experimental data, e.g., for a starting P of 300 MPa: ~7.33 wt% H_2O (Holtz et al. 1995) or ~7.10 wt% H_2O (Jaupart and Tait 1990), and for final P of 50 MPa: ~2.36 wt% H_2O (Holtz et al. 1995), ~2.4 wt% H_2O (Yamashita 1999), or ~2.90 wt% H_2O (Jaupart and Tait 1990).

The calculated BND values plotted in Figure 4b show a clear trend of increasing BND for the samples from continuous to multi-step and to single-step decompression methods (Table 1, Fig. 4b). The BSD curves of our experimental products show three different trends as illustrated in Figure 5. The BSD curve for the sample of the single-step decompression shows the largest variations both in the size of the bubbles and in the population number density, if it is compared with the other two samples. This sample contains the largest proportion of small bubbles. The BSD trend for the sample of multi-step decompression shows the smallest variations between the size and the population density of bubbles, whereas the BSD of continuously decompressed sample shows a very flat curve in Figure 5, indicating similar proportions of bubbles with different size.

DISCUSSION

Comparison of decompression methods

The observation that the BND values of the sample increase from continuous decompression to multi-step decompression and to single-step decompression provides important constraints on the mechanism of bubble formation. Changes in the BND values combined with BSD and porosity (or vesicularity) data give information on the processes of nucleation and growth of bubbles in the systems having different decompression history. At a given volume of the sample and given total porosity, the BND value is an indication for the relative number of bubbles. Hence, the difference in BND reflects the efficiency of bubble production or nucleation on decompression.

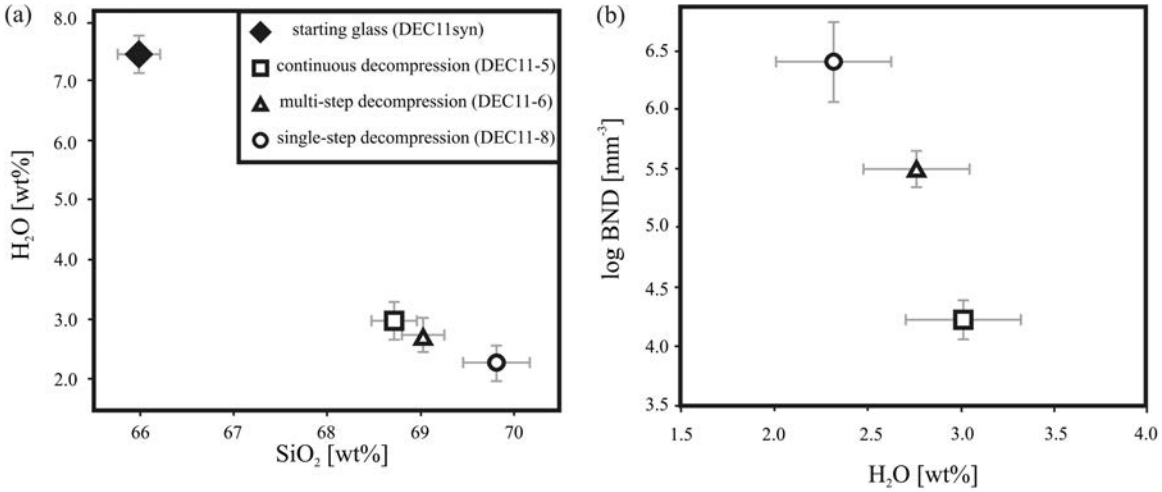

FIGURE 4. Experimental results of the chemical and textural analyses. (**a**) SiO_2 content plotted against H_2O content of the residual melts of the starting and decompression experiments. (**b**) H_2O content vs. log BND, plotted for decompression experiments only.

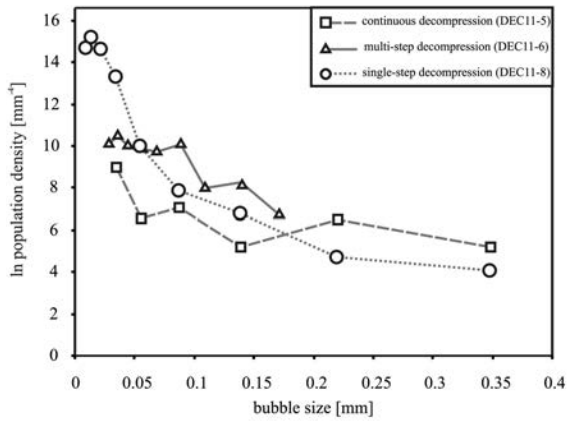

FIGURE 5. Bubble size distribution, calculated following the method of Higgins (2000), in samples after decompression experiments.

Bubbles can either nucleate homogeneously or heterogeneously in a supersaturated melt. As the fluid-saturated starting glass synthesized at 300 MPa and 1050 °C was nearly crystal- and bubble-free (Fig. 3a), homogeneous bubble nucleation is expected to be the primary process in the decompression experiments. In the case of homogeneous bubble nucleation, small clusters of gas molecules form the so-called bubble embryos. Dependent on the free energy, associated with the formation of the separate gas phase, and on the interfacial energy, associated with the creation of the bubble surface, a bubble embryo can grow or can shrink (see review of Sparks et al. 1994). An embryo can only grow when the critical radius (r_c) is overcome by adding one extra molecule to the cluster. r_c is given by:

$$r_c = 2\sigma/\Delta P \quad (5)$$

where σ is the interfacial tension (also referred to as melt-vapor surface tensions; e.g., Mangan and Sisson 2005) and ΔP is the supersaturation pressure (i.e., difference between gas pressure in the melt and the ambient pressure). Mangan and Sisson (2005) showed that as water exsolves and the melt evolves to more silicic compositions, the melt-vapor surface tensions (σ) increases, thus lowering the bubble nucleation rate and ultimately the number of bubbles produced. On the other hand, the higher the supersaturation pressure, the lower the critical size of an embryo, facilitating nucleation.

The nucleation pressure (*Pn*) was not directly determined for our experimental setup, for example by intermediate runs, that would provide further information on the origin of the bubble nucleation process (heterogeneous or homogeneous). The *Pn* value can be used as a criterion characterizing the nucleation process, i.e., pressure difference (ΔP) between the starting pressure and *Pn* as little as ~5 MPa is indicative of heterogeneous nucleation, whereas greater ΔP values (i.e., lower *Pn*) would imply homogeneous nucleation (e.g., Sparks et al. 1994).

In our single-step decompression experiment, the oversaturation produced by instantaneous pressure drop of 250 MPa is definitely high enough for nucleation as evidenced by high BND values. In the run with continuous decompression the bubbles were nucleated only when certain oversaturation pressure was reached (*Pn*: here unknown). During further continuous decompression the exsolved water would rather diffuse into the already existing bubbles and let those bubbles grow due to favorable energetics, than accumulate into new clusters that could result in new nucleation (see review of Sparks et al. 1994) explaining the relatively low BND values. *Pn* in our multi-step decompressions experiments was probably higher than during continuous but lower than during single-step decompression as we decompress by 50 MPa steps (Fig. 2), resulting in intermediate BND values.

It must be noted that the experimental product of the single-step decompression experiment (Fig. 3d) differs clearly from that of the continuous and stepwise decompression experiment. A segment of a big bubble can be seen at the right hand side of the sample surrounded by smaller deformed bubbles of different generations and sizes. Some kind of channel structure crosscutting the bubbles is also observed. We suggest two processes that influenced the degassing and bubble texture of the single-step experiment: (1) secondary sudden growth of a preexisting bubble, already present in the starting glass that led to an elongation and bending of the surrounding smaller bubbles, and (2) channel formation in the sample of single-step decompression that may indicate fluid escape from over-pressurized bubbles through the melt (Fig. 3d). The channel is quite different from cracks formed in the glassy state during quenching or preparing the sample for analysis. The channel is much broader than the fine glass cracks in Figure 3b, the edges of the channel are rounded, and the two halves cannot be merged perfectly. We calculated a viscosity of 10^3 Pa·s and a relaxation time of 10^{-7} s for the liquid glass transition of the rhyodacitic melt at 1050 °C using the viscosity model for hydrous dacitic liquids of Whittington et al. (2009) and the relaxation model of Dingwell and Webb (1990). Although relaxation time of the melt is in the range of microseconds, sudden bubble formation and growth at high fluid supersaturation resulting in high fluid overpressure may have formed the observed channel due to fluid escape from over-pressurized bubbles through the melt for pressure relief. To the best of our knowledge the observed channel formation in melt had as yet not been shown experimentally.

Bubble growth can take place during decompression due to either gas diffusion from a supersaturated melt into the bubble and due to expansion of existing gas bubbles as pressure reduces (Sparks et al. 1994). The effects of surface tension, of melt viscosity and of inertia can hinder the growth of bubbles. The high BND measured in the decompressed samples evidences the dominance of the bubble nucleation process, resulting in higher number of relatively small-sized bubbles (compare BND and BSD, Table 1 and Figs. 4b and 5). Due to the sudden drop in pressure of 250 MPa within the first few seconds equal to an ascent rate of 1500 km/h of the single-step decompression experiment, the melt became highly water-supersaturated at the final pressure of 50 MPa. At these conditions, the critical size of bubble embryo (Sparks et al. 1994) was dramatically reduced due to a high supersaturation pressure (ΔP) and relatively initial low melt-vapor surface tensions (σ; Mangan and Sisson 2005). Thus, enhanced volatile exsolution (Hurwitz and Navon 1994) led to major bubble nucleation in the system. In contrast, bubble growth was the dominant bubble-forming process (Gardner

2007a, 2007b) in the continuously decompressed system, indicated by the low BND value and the large average bubble size when compared to multi-step or single-step decompression runs (Figs. 4b and 5). At the beginning of the continuous decompression, bubble nucleation and therefore water exsolution can only start when *Pn* is overcome. During the ongoing continuous pressure release and therefore continuous water exsolution from the melt, no significant oversaturation was reached for a given time interval, precluding further nucleation of bubbles. Hence, water diffused instead into already existing bubbles, whereas probably only a few new bubbles nucleated, undergoing continuous growth and coalescence during decompression. Thus, the single-step and continuous decompression paths represent two extreme cases in which bubble nucleation and bubble growth are predominant processes, respectively. In this sense, the multi-step decompression method represents the intermediate case between rapid and slow pressure release in magmatic system.

In comparison to the water solubility of high-silica melts at 1050 °C and 50 MPa of ~2.4 wt% H_2O (e.g., Holtz et al. 1995; Yamashita 1999), it seems that the total loss of water is more effective in the course of single drop of pressure than in the other cases, indicating that rapid magma ascent or quick pressure release with a subsequent long dwell time at low pressures will result in more efficient magma degassing, although it has to be noted that these changes in the determined water contents of the residual melts (by NIR) are within the uncertainties (±0.3 wt%) and may be used for qualitative discussion only.

Implication for natural systems

During magma ascent in volcanic conduits, the magma can change its physical and chemical properties either continuously or step-wise due to changes in *P-T* conditions, water exsolution rate, bubble-forming and crystallization processes (e.g., Hurwitz and Navon 1994). These variations have a major impact on the rheological and dynamic behavior of the magma and therefore also on the magma ascent paths and rates (e.g., Ida 1996; Melnik and Sparks 1999; Maeda 2000). Thus, there is a self-sustaining feedback between the physicochemical and flow properties of the magma and *P-T-t* conditions. Another external parameter, potentially influencing magma ascent rate, can be the conduit diameter, which is probably not constant over the entire distance from magma chamber to the volcanic vent (e.g., Noguchi et al. 2008). Therefore, we can expect a broad range of decompression rates from the onset of magma ascent at depth until the actual eruption at the surface, as well as changing ascent velocities with time due to variation in the magma supply from below. The data obtained in our study clearly show that the manner and efficiency of fluid exsolution are strongly dependent on the style of decompression. The most reactive system, in terms of bubble proportion and the amount of exsolved fluid, is expected to develop in eruptions with very rapid pressure release, for instance, in Plinian eruptions (Hamada et al. 2010) or in catastrophic caldera-forming events. All described decompression styles can be simulated with the new developed valve connected to the IHPV including decompression-induced crystallization. This new high-tech tool will give new insights to the mechanisms of ascending magmas.

Acknowledgments

We thank Barbara Meyer for technical assistance and the reviewers Caroline Martel and Jim Gardner for helpful comments. This study is supported by the DFG NO 378/5 and HO 1337/16, as well as supported by the EU SLS 20090928.

References cited

Alidibirov, M. and Dingwell, D.B. (1996) Magma fragmentation by rapid decompression. Nature, 380, 146–148.

Armienti, P. (2008) Decryption of igneous rock textures: crystal size distribution tools. In K.D. Putirka and F.J. Tepley III, Eds., Minerals, Inclusions and Volcanic Processes, 69, p. 623–649. Reviews in Mineralogy and Geochemistry, Mineralogical Society of America, Chantilly, Virginia.

Berndt, J., Liebske, C., Holtz, F., Freise, M., Nowak, M., Ziegenbein, D., Hurkuck, W., and Koepke, J. (2002) A combined rapid-quench and H_2-membrane setup for internally heated pressure vessels: Description and application for water solubility in basaltic melts. American Mineralogist, 87, 1717–1726.

Botcharnikov, R.E., Behrens, H., Holtz, F., Koepke, J., and Sato, H. (2004) Sulfur and chlorine solubility in Mt. Unzen rhyodacitic melt at 850°C and 200 MPa. Chemical Geology, 213, 207–225.

Brugger, C.R. and Hammer, J.E. (2010) Crystallisation kinetics in continuous decompression experiments: implications for interpreting natural magma ascent processes. Journal of Petrology, 51, 1941–1965.

Cichy, S.B., Botcharnikov, R.E., Holtz, F., and Behrens, H. (2011) Vesiculation and microlite crystallization induced by decompression: a case study of the 1991–1995 Mt Unzen eruption (Japan). Journal of Petrology, in press, DOI: 10.1093/petrology/egq072.

Dingwell, D.B. and Webb, S.L. (1990) Relaxation in silicate melts. European Journal of Mineralogy, 2, 427–449.

Freise, M., Holtz, F., Nowak, M., Strauss, H., and Scoates, J.S. (2009) Differentiation and crystallization conditions of basalts from the Kerguelen large igneous province: an experimental study. Contributions to Mineralogy and Petrology, 158, 505–527.

Gardner, J.E. (2007a) Heterogeneous bubble nucleation in highly viscous silicate melts during instantaneous decompression from high pressure. Chemical Geology, 236, 1–12.

——— (2007b) Bubble coalescence in rhyolitic melts during decompression from high pressure. Journal of Volcanology and Geothermal Research, 166, 161–176.

Gardner, J.E., Hilton, M., and Carroll, M.R. (1999) Experimental constraints on degassing of magma: isothermal bubble growth during continuous decompression from high pressure. Earth and Planetary Science Letters, 168, 201–218.

Giordano, D., Potuzak, M., Romano, C., Dingwell, D., and Nowak, M. (2008) Viscosity and glass transition temperature of hydrous melts in the system $CaAl_2Si_2O_8$-$CaMgSi_2O_6$-H_2O. Chemical Geology, 256, 203–215.

Gonnermann, H.M. and Manga, M. (2005) Nonequilibrium magma degassing: Results from modelling of the ca. 1340 A.D. eruption of Mono Craters, California. Earth and Planetary Science Letters, 238, 1–16.

——— (2007) The fluid mechanics inside a volcano. Annual Reviews of Fluid Mechanics, 39, 321–356.

Hamada, M., Laporte, D., Cluzel, N., Koga, K.T., and Kawamoto, T. (2010) Simulating bubble number density of rhyolitic pumices from Plinian eruptions: constraints from fast decompression experiments. Bulletin of Volcanology, 72, 735–746.

Hawkesworth, C., George, R., Turner, S., and Zellmer, G. (2004) Time scales of magmatic processes. Earth and Planetary Science Letters, 218, 1–16.

Herd, R.A. and Pinkerton, H. (1997) Bubble coalescence in basaltic lava: Its impact on the evolution of bubble populations. Journal of Volcanology and Geothermal Research, 75, 137–157.

Higgins, M.D. (2000) Measurement of crystal size distribution. American Mineralogist, 85, 1105–1116.

——— (2002) Closure in crystal size distributions (CSD), verification of CSD calculations, and the significance of CSD fans. American Mineralogist, 87, 171–175.

——— (2006a) Verification of ideal semi-logarithmic, lognormal or fractal crystal size distributions from 2D datasets. Journal of Volcanology and Geothermal Research, 154, 8–16.

——— (2006b) Quantitative Textural Measurements in Igneous and Metamorphic Petrology, 276 p. Cambridge University Press, U.K.

Holtz, F., Behrens, H., and Dingwell, D.B., and Johannes, W. (1995) Water solubility in haplogranitic melts. Compositional, pressure and temperature dependence. American Mineralogist, 80, 94–108.

Hurwitz, S. and Navon, O. (1994) Bubble nucleation in rhyolitic melts: experiments at high pressure, temperature and water content. Earth and Planetary Science Letters, 122, 267–280.

Ida, Y. (1996) Cyclic fluid effusion accompanied by pressure change: implication for volcanic eruptions and tremor. Geophysical Research Letters, 23, 1457–1460.

Jaupart, C. and Tait, S. (1990) Dynamics of eruptive phenomena. In J. Nicholls and J.K. Russell, Eds., Modern Methods of Igneous Petrology: Understanding Magmatic Processes, 24, p. 213–238. Reviews in Mineralogy, Mineralogical Society of America, Chantilly, Virginia.

Maeda, I. (2000) Nonlinearvisco-elastic volcanic model and its application to the recent eruption of Mt. Unzen. Journal of Volcanology and Geothermal Research, 95, 35–47.

Mangan, M. and Sisson, T. (2000) Delayed, disequilibrium degassing in rhyolite magma: decompression experiments and implications for explosive volcanism. Earth and Planetary Science Letters, 183, 441–455.

——— (2005) Evolution of melt-vapor surface tension in silicic volcanic systems: experiments with hydrous melts. Journal of Geophysical Research, 110, B01202, DOI: 10.1029/2004JB003215.

Marsh, B.D. (1988) Crystal size distribution (CSD) in rocks and the kinetics and dynamics of crystallization. I. Theory. Contributions to Mineralogy and Petrology, 99, 277–291.

Martel, C. and Schmidt, B.C. (2003) Decompression experiments as an insight into ascent rates of silicic magmas. Contributions to Mineralogy and Petrology, 144, 397–415.

Mastrolorenzo, G. and Pappalardo, L. (2006) Magma degassing and crystallization processes during eruptions of high-risk Neapolitan-volcanoes: Evidence of common equilibrium rising processes in alkaline magmas. Earth and Planetary Science Letters, 250, 164–181.

Melnik, O. and Sparks, R.S.J. (1999) Nonlinear dynamics of lava dome extrusion. Nature, 402, 37–41.

Miller, C.F. and Wark, D.A. (2008) Supervolcanoes and their explosive supererruptions. Elements, 4, 11–16.

Noguchi, S., Toramaru, A., and Nakada, S. (2008) Relation between microlite textures and discharge rate during the 1991–1995 eruptions at Unzen, Japan. Journal of Volcanology and Geothermal Research, 175, 141–155.

Nowak, M., Schreen, D., and Spickenbom, K. (2004) Ar and CO_2 on the race track in silicate melts: a tool for the development of a CO_2 speciation and diffusion model. Geochimica et Cosmochimica Acta, 68, 5127–5138.

Ohlhorst, S., Behrens, H., and Holtz, F. (2001) Compositional dependence of molar absorptivities of near-infrared OH- and H_2O bands in rhyolitic to basaltic glasses. Chemical Geology, 174, 5–20.

Sato, H., Nakada, S., Fujii, T., Nakamura, M., and Suzuki-Kamata, K. (1999) Groundmass pargasite in the 1991-1995 dacite of Unzen volcano: phase stability experiments and volcanological implications. Journal of Volcanology and Geothermal Research, 89, 197–212.

Sato, H., Holtz, F., Behrens, H., Botcharnikov, R.E., and Nakada, S. (2005) Experimental petrology of the 1991-1995 dacite of Unzen volcano. Part II: Cl/OH partitioning between hornblende and melt and its implications for the origin of oscillatory zoning of hornblende phenocryst. Journal of Petrology, 46, 339–354.

Scheu, B., Spieler, O., and Dingwell, D.B. (2006) Dynamics of explosive volcanism at Unzen volcano: an experimental contribution. Bulletin of Volcanology, 69, 175–187.

Sparks, R.S.J., Barclay, J., Jaupart, C., Mader, H.M., and Phillips, J.C. (1994) Physical aspects of magma degassing I. Experimental and theoretical constraints on vesiculation. In M.R. Carroll and J.R. Holloway, Eds., Volatiles in Magmas, 30, p. 412–445. Reviews in Mineralogy, Mineralogical Society of America, Chantilly, Virginia.

Spickenbom, K., Sierralta, M., and Nowak, M. (2010) Carbon dioxide and Argon diffusion in silicate melts: insights into the CO_2 speciation in magmas. Geochimica et Cosmochimica Acta, 74, 6541–6564.

Spieler, O., Kennedy, B., Kueppers, U., Dingwell, D.B., Scheu, B., and Taddeucci, J. (2004) The fragmentation threshold of pyroclastic rocks. Earth and Planetary Science Letters, 226, 139–148.

Stelling, J., Botcharnikov, R.E., Beermann, O., and Nowak, M. (2008) Solubility of H_2O- and chlorine-bearing fluids in basaltic melt of Mount Etna at T=1050-1250°C and P=200 MPa. Chemical Geology, 256, 102–110.

Symonds, R.B., William, R.I., Gregg, B.J.S., and Gerlach, T.M. (1994) Volcanic-gas studies: methods, results and applications. In M.R. Carroll and J.R. Holloway, Eds., Volatiles in Magmas, 30, p. 1–66. Reviews in Mineralogy, Mineralogical Society of America, Chantilly, Virginia.

Whittington, A.G., Hellwig, B.M., Behrens, H., Joachim, B., Stechern, A., and Vetere, F. (2009) The viscosity of hydrous dacitic liquids: implications for the rheology of evolving silicic magmas. Bulletin of Volcanology, 71, 185–199.

Withers, A.C. and Behrens, H. (1999) Temperature-induced changes in the NIR spectra of hydrous albitic and rhyolitic glasses between 300 and 100 K. Physics and Chemistry of Minerals, 27, 119–132.

Woods, A.W. (1995) The dynamics of explosive volcanic eruptions. Reviews in Geophysics, 33, 495–530.

Woods, A.W. and Koyaguchi, T. (1995) Transitions between explosive and effusive eruptions. Nature, 370, 641–644.

Yamashita, S. (1999) Experimental study of the effect of temperature on water solubility in natural rhyolite melt to 100 MPa. Journal of Petrology, 40, 1497–1507.

Manuscript received January 14, 2011
Manuscript accepted April 29, 2011
Manuscript handled by Daniel Neuville